Journal of Energy Storage 179 (2026) 123841

Contents lists available at ScienceDirect

Journal of Energy Storage

journal homepage: www.elsevier.com/locate/est

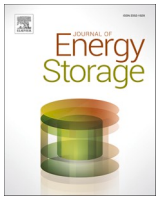

Research papers

Nanoscale thermal behavior and phase transition of nano-enhanced phase change materials in ribbed channels: A molecular dynamics study

Jialing Li [a], Xiaogui Gou [b,*], Mahmut Taner [c], Soheil Salahshour [d,e,f,g], N. Emami [h,*], Mustafa Bayram [i]

[a] Chongqing Youth Vocational & Technical College, Chongqing, 401320, China
[b] College of Intelligent Manufacturing, Chongqing Institute Of Engineering, Chongqing, 400056, China
[c] Faculty of Engineering and Architecture, Istanbul Gelisim University, Istanbul, Türkiye
[d] Faculty of Engineering and Natural Sciences, Istanbul Okan University, Istanbul, Turkey
[e] Faculty of Engineering and Natural Sciences, Bahcesehir University, Istanbul, Turkey
[f] Research Center of Applied Mathematics, Khazar University, Baku, Azerbaijan
[g] Faculty of Science and Letters, Piri Reis University, Tuzla, Istanbul, Turkey
[h] Fast Computing Center, Shabihsazan Ati Pars, Tehran, Iran
[i] Department of Computer Engineering, Biruni University, 34010, Istanbul, Turkey

ARTICLE INFO

Keywords:
Thermal behavior
Phase change material
Nanoparticles
Molecular dynamics simulation

ABSTRACT

Ribbed channel geometries are widely recognized for their ability to modify flow structures and influence thermal transport. In this study, the nanoscale thermal behavior of nano-enhanced phase change materials (NePCMs) confined within a ribbed nanochannel was investigated using molecular dynamics simulations. The model consisted of a confined domain ($50 \times 150 \times 50$ Å^3) with non-connected rotating ribs, and the effect of rib number (1–4) on atomic-level structural and thermal properties was systematically analyzed over a 10 ns simulation period. The results show that increasing the number of ribs altered local atomic arrangements, enhanced fluid–structure interactions, and intensified velocity fluctuations within the confined region. These effects led to measurable, statistically significant improvements in thermal transport. Specifically, heat flux increased from 5.19 ± 0.02 to 5.54 ± 0.01 W/m^2 (approximately 6.7%), while thermal conductivity increased from 0.65 ± 0.01 to 0.72 ± 0.02 W/m·K (approximately 10.8%) as the rib number increased from 1 to 4. In addition, the phase transition time was slightly reduced, indicating faster energy absorption and release dynamics under enhanced mixing and interfacial interaction conditions. It should be noted that the findings provide atomistic-level insight into how internal geometric features influence heat transfer and phase transition mechanisms. These results contribute to the fundamental understanding of nanoscale transport phenomena and may inform future multiscale design strategies for advanced thermal management systems.

1. Introduction

Effective thermal management plays a crucial role across various technological domains, such as electronics cooling, renewable energy systems, and the regulation of building temperatures (T) [1]. As contemporary devices and systems grow increasingly powerful and compact, the need for efficient heat control and dissipation becomes vital to maintain performance, reliability, and safety [2]. In the realm of renewable Energy, effective thermal management improves the efficiency of energy conversion processes. It also extends the lifespan of components such as solar panels and batteries. In the field of electronics, it mitigates overheating that could impair functionality and lead to failures [3,4]. Moreover, in building applications, thermal regulation directly affects energy consumption and indoor comfort [5]. Thus, improving heat transfer (HT) and energy storage materials, such as phase change materials (PCMs), by incorporating nanoparticles and

Abbreviations: PCMs, Phase change materials; HT, Heat transfer; HF, Heat flux; TC, Thermal conductivity; MD, Molecular dynamics; CT, Charge time; DT, Discharge time; LJ, Lennard-Jones; D, Density; V, Velocity; T, Temperature; NVT, Canonical ensemble; NVE, Microcanonical ensemble; CNT, Carbon nanotube; GNPs, Graphene nanoplatelet; RDF, Radial distribution function.

* Corresponding authors.
E-mail addresses: gouxiaogui@cqie.cn (X. Gou), soheil.salahshour1361@gmail.com (S. Salahshour), nafise.emami@iaukhsh.ac.ir (N. Emami).

https://doi.org/10.1016/j.est.2026.123841
Received 4 November 2025; Received in revised form 15 June 2026; Accepted 21 July 2026
Available online 30 July 2026

optimizing structural features, is vital for advancing sustainable, high-efficiency thermal management solutions [6,7]. Paraffin wax is extensively utilized as a PCM owing to its substantial latent heat of fusion, chemical stability, minimal supercooling, and safety; it effectively absorbs and releases considerable amounts of thermal Energy during the processes of melting and solidification, rendering it a proficient medium for thermal energy storage and T regulation across diverse applications [8].

Recent research has demonstrated notable progress in enhancing the thermal conductivity (TC), T response, and storage capacity of PCMs by incorporating various nanoparticles. Furthermore, these studies have highlighted the importance of addressing nanoparticle dispersion mechanisms, multi-cycle performance, and geometric optimizations, including nanochannel designs and ribs, to enhance HT efficiency [9]. For instance, Agarwal et al. [10] revealed that integrating structured porous materials with phase change composites significantly enhanced heat absorption behavior and thermal performance in heat sink systems, highlighting the growing importance of engineered PCM structures in advanced thermal energy storage applications. Ru et al. [11] investigated the effect of nanoparticle size on the thermal performance of a paraffin/O_2/Al_2O_3 hybrid heat sink using molecular dynamics (MD) simulation. They found that increasing nanoparticle size improved the system's TC. Qing et al. [12] used simulations to show that, in silica aerogel/paraffin nanostructures, increasing the size of copper oxide nanoparticles decreased density (D) and TC, thereby affecting the charging and discharging behavior of PCMs. Zhao et al. [13] found that thicker silica nanolayers in silica-paraffin composites reduced melting enthalpy. However, by enhancing molecular interactions, they improved TC, revealing the trade-off between structure and HT. Using carbon-based nanomaterials and metal oxide nanoparticles also showed promise for tuning PCM properties. Wu et al. [14] observed significant improvements in specific heat, TC, and storage capacity when Al_2O_3 nanoparticles were added to molten-salt PCMs, demonstrating that nanoparticle additives can optimize thermal energy storage.

Building upon these advances, the present study aimed to investigate the nanoscale thermal behavior of nanoparticle-enhanced phase change materials (NePCMs) confined within rib-structured nanochannels, with particular emphasis on the role of non-connected rotating ribs, a structural feature that received limited attention in previous studies. Using MD simulations, this work systematically examined how variations in rib number influenced key thermophysical properties, including D, velocity (V), T, heat flux (HF), and TC at the atomic scale. Unlike prior studies that primarily focus on material composition, this work emphasizes the role of internal geometric features in shaping atomic trajectories, intermolecular interactions, and energy-transfer pathways within confined environments. The presence of rotating ribs induced localized perturbations in particle motion, leading to increased V fluctuations, enhanced collision frequency, and stronger momentum exchange among particles, thereby influencing phase transition dynamics and thermal transport behavior. It should be noted that the present study was conducted at the nanoscale, and the results were intended to provide fundamental insight into the structure–property relationships governing HT and phase-change behavior under confinement. Rather than relying on continuum-scale interpretations, the analysis was based on atomistic mechanisms derived from MD simulations. The findings, therefore, contributed to a deeper understanding of nanoscale transport phenomena and may serve as a foundation for future multiscale investigations aimed at connecting atomistic behavior with larger-scale thermal systems. Based on these considerations, the present study was guided by the hypothesis that increasing the number of rotating ribs within a confined nanochannel induces systematic perturbations in atomic motion, thereby enhancing V fluctuations, intermolecular interactions, and momentum exchange within the nanoparticle-enhanced PCM. It was further hypothesized that these atomistic effects resulted in measurable and systematic variations in thermal transport properties, including HF and TC, as well as modifications in phase transition dynamics.

2. Simulation method

In this study, an atomic-scale model of a nanochannel with embedded rotating ribs was constructed to investigate the thermal behavior and phase change dynamics of paraffin-based PCMs enhanced with Cu NPs. The dimensions of the simulation box were set to 50 × 150 × 50 Å^3. To model the initial structure, Avogadro [15] was used to model paraffin, Cu nanoparticles, and ribs (with carbon particles), and Packmol [16] was used to extend and pack the structures. LAMMPS software [17] was used to model carbon walls. Boundary conditions were set as fixed (non-periodic) in the x-direction and periodic in y- and z-directions. Periodic boundary conditions (PBCs) in MD simulations effectively model an infinite system by replicating the simulation cell in all spatial directions, eliminating edge effects and enabling accurate representation of bulk material behavior at the atomic scale. Although the simulations were performed on nanoscale volumes, using PBCs ensured that the local structural, thermal, and flow properties exhibited intrinsic bulk-phase change and thermal transport characteristics. These atomic-scale insights and equations describing TC, HF, and phase-transition dynamics can be scaled up using multiscale modeling frameworks or continuum-based models to inform and optimize macroscopic thermal management systems [18]. MD simulation settings in current computational research are given in Table 1. Fig. 1 shows a schematic of the modeled structure. The flow within the nanochannel was simulated by applying external forces directly to the paraffin-Cu nanoparticle fluid atoms, thereby inducing fluid motion and shear and replicating physical flow conditions at the nanoscale. These forces were implemented using ‘fix addforce’ and ‘fix efield’ commands [19] available in LAMMPS, applying both constant and time-dependent sinusoidal components to mimic flow-induced mechanical shear. The ribs inside the channel were modeled as atom groups rotating around the channel axis via discrete angular increments, generated by ‘displace_atoms’ command [19] (around the tube's longitudinal (z) axis by discrete angular increments (e.g., −15°)). In this simulation setting, the rotated sample underwent a displacement process with an intensity of 75,000 degrees/ns. This setting enabled the designed system to be suitable for ultrafast HT conditions [20,21]. In actual cases, these proposed systems can be implemented to enhance microfluidic convection and nanoparticle-mediated heat transfer in advanced cooling systems, such as those for quantum computing components. This combined approach created complex convective flow patterns and enhanced interaction between rotating ribs and the nanoparticle-enhanced PCM, enabling realistic modeling of HT phenomena. MD simulations using external forcing to induce flow were a well-established method to investigate fluid dynamics and thermal transport in nanochannels, providing insights into nanoscale V profiles, D fluctuations, and energy transport that were difficult to capture with continuum methods [22–24]. Initially, the system was equilibrated at 300 K under the canonical ensemble (NVT) using a Nose-Hoover thermostat for 10 ns. To ensure equilibrium in MD simulations, the time evolution of key system properties, such as

Table 1
MD simulation settings in current computational research.

Computational Parameter	Parameter Ratio/Setting
MD Box Length	50 × 150 × 50 Å^3
Boundary condition	F P P
Number of Atoms	14,000
Time Step	0.01 fs
Initial T	300 K
Damping T	1
Ensemble	NVE/NVT
Force field	Lennard-Jones/C
Equilibrium Time	10 ns
Total MD Time	20 ns

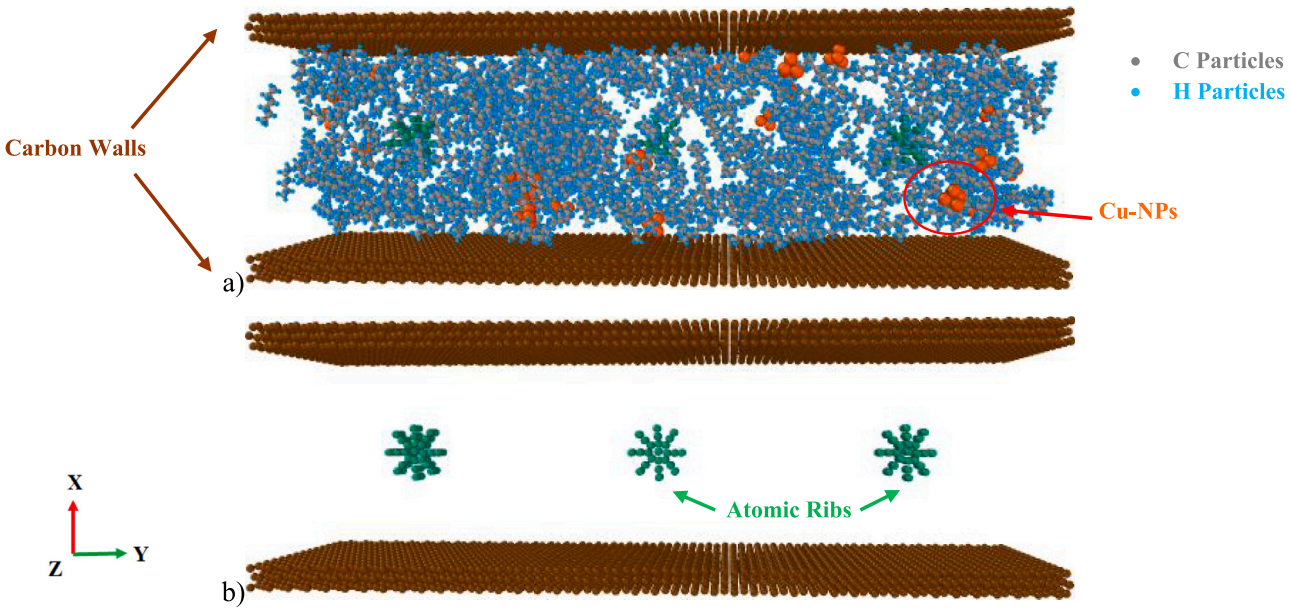

Fig. 1. Schematic of the simulated nanochannel structure in the MD study: (a) with paraffin and (b) without paraffin. Gray and blue spheres represent carbon and hydrogen atoms in paraffin, green spheres represent atoms forming the ribs, and brown indicates carbon nanochannel walls. (For interpretation of the references to colour in this figure legend, the reader is referred to the web version of this article.)

potential Energy, was analyzed. Subsequently, the ensemble switched to microcanonical (NVE) to simulate phase change behavior during a 10 ns production run. To model rib rotation within the nanochannel, the ribs were explicitly constructed from groups of atoms arranged in fixed volumetric regions (shown as green atoms in Fig. 1). The total simulation time of 20 ns with a very fine timestep of 0.01 fs guaranteed the high temporal resolution necessary to capture ultrafast atomic motions and thermal transport processes at the nanoscale. As reported in previous research, a small time step (0.01 fs) yielded more accurate outputs, accessible from standard MD simulations [25]. Additionally, each MD simulation was repeated five times, and the average value of outputs was reported to minimize computational errors. Technically, this process was done by repeating the run procedure of LAMMPS script by changing the "SEED" numbers inside them.

2.1. Force field details

The interaction potentials used in this MD study combined Lennard-Jones (LJ) and Coulombic potentials to accurately represent atomic-level forces among paraffin molecules, Cu NPs, carbon walls, and rib atoms. Specifically, force field parameters (including LJ well depth (ε) and size parameter (σ) for different atom pairs, as well as partial atomic charges for electrostatic interactions) were adopted and validated based on extensive prior literature and parameter sets commonly used for similar molecular systems [26,27]. The combined potential energy function U(rij) employed is given by the sum of LJ [28,29] and Coulomb [30] potentials as:

$$U_{ij}(r) = 4\varepsilon_{ij}\left[\left(\frac{\sigma_{ij}}{r_{ij}}\right)^{12} - \left(\frac{\sigma_{ij}}{r_{ij}}\right)^{6}\right] + \frac{-1}{4\pi\varepsilon_0}\frac{q_i q_j}{r_{ij}^2} \quad (1)$$

where r is the distance among the particles, ε represents the depth of the potential well, and σ is the finite distance at which the potential is zero. The parameters ε_{ij} and σ_{ij} are calculated as [31]:

$$\varepsilon_{ij} = \sqrt{\varepsilon_i \varepsilon_j} \quad (2)$$

$$\sigma_{ij} = \frac{\sigma_i + \sigma_j}{2} \quad (3)$$

The parameters of the LJ potential function for the present particles [26,27] are given in Table 2. LJ parameters for the particles, such as copper, were adopted from general-purpose force fields, such as DREIDING and UFF, which provide standardized parameters based on typical chemical environments. While these parameters were widely used and served as a reasonable initial point, they were not specifically optimized for Cu-paraffin interactions, which did not account for environment-dependent effects, such as polarization or specific metal-organic coordination. The literature acknowledged that UFF and DREIDING assign one parameter set per element, which may limit accuracy for some complex interactions. Ideally, these parameters should be validated or refined by comparing simulation results to experimental data or higher-level theoretical calculations. In the absence of such data, using these parameters and their potential limitations was transparently acknowledged as a current practical approximation commonly accepted in molecular simulations involving metals [32,33]. The harmonic potential in LAMMPS models represents covalent bond stretching and bending by assuming a quadratic energy function of deviations from equilibrium values, following Hooke's Law. For bonds, the potential energy V bond is given by [34]:

$$V_{bond} = \frac{1}{2}k(r - r_0)^2 \quad (4)$$

where r is the bond length, r_0 is the equilibrium bond length, and k is the force constant indicating bond strength. This approach accurately represented bond stretching if correctly implemented in LAMMPS. Similarly, atomic angles were modeled with a harmonic potential for bending [35]:

$$V_{\text{angle}} = \frac{1}{2}k_\theta(\theta - \theta_0)^2 \quad (5)$$

With θ is the current angle, θ_0 is the equilibrium angle, and k_θ is the

Table 2
The parameters of the LJ potential function for the present particles [26,27].

Particles	ε (kcal/mol)	σ (Å)
C	0.105	3.851
H	0.044	2.886
Cu	0.005	3.495

bending force constant. This allowed LAMMPS to capture molecular shape changes and dynamics effectively. The specific bond and angle parameters depended on the system and are outlined in detail in the relevant interaction tables. Finally, the electrostatic interaction is defined by Coulomb's law and the partial charges of each atom, estimated using the Online Atomic Charge Calculator [36]. The equilibrium distance in a simple bond interaction is given in Table 3. Also, the equilibrium angles in angular bond interaction are given in Table 4.

2.2. Equilibration process

The convergence of potential Energy to a stable, nearly constant value over time was a strong indicator that the system equilibrated. Fig. 2 represents the change in potential Energy over 10 ns. Monitoring the potential energy curve during the initial equilibration phase (under the NVT ensemble) revealed that, after some fluctuations at early times, the potential Energy stabilized around a constant value, as illustrated in the figure. This plateau in potential Energy indicated that the atomic system relaxed into an equilibrium state in which energy exchanges balanced. Numerically, the potential Energy of the atomic sample stabilized at 1.42 kcal/mol after 10 ns of simulation.

3. Radial distribution function

After equilibrating the initial paraffin sample, we validated the computational method to ensure the accuracy and physical reliability of simulation outputs. The system consisted of pure paraffin molecules contained in a simulation box with periodic boundary conditions applied in all three spatial directions, thereby mimicking a bulk environment without explicit solid walls. Under these conditions, the paraffin remained in the liquid phase at simulation T, consistent with its melting point and reported physical phase behavior in the literature. The radial distribution function (RDF) of paraffin molecules at the final stage of the equilibrium process is shown in Fig. 3. The RDF was computed between the carbon atoms of adjacent paraffin molecules, providing a measure of average atomic spatial distribution around a reference atom. This function characterized short- and medium-range order, indicating the local structural organization in the simulated liquid. Furthermore, the calculated RDF pattern remained consistent before and after the HT procedure (as shown in Fig. 3), indicating the structural stability of the paraffin PCM throughout the simulated thermal process. This temporal stability of the RDF profile supported the robustness and reproducibility of our MD simulation approach. Fig. 3b shows a good match between the simulated and experimental RDFs, validating that the chosen computational method accurately captures the structural properties of paraffin as a PCM [37]. The slight differences in the RDF peaks compared to the reference may stem from inherent limitations and approximations in the force field used in the simulation. Force fields, which defined the potential energy functions and parameters for atomic interactions, were typically parameterized to reproduce specific experimental or ab initio data. However, they may not perfectly capture all aspects of molecular structure and dynamics. Variations in LJ parameters, electrostatic terms, or bond-stretching potentials can shift peak height and position in RDFs. Additionally, the force field may under- or overestimate specific attractive or repulsive interactions, thereby affecting local atomic packing and coordination, as reflected in RDF peaks. Such deviations were common and highlighted the need for ongoing force-field refinement or reparameterization to improve accuracy, potentially including fitting to RDF data directly or incorporating higher-level quantum-mechanical calculations. Despite these discrepancies, the overall agreement validated the force field's ability to capture key structural behaviors relevant to the study system [38–40].

Table 3
The equilibrium distance in a simple bond interaction.

Bond Type	Bonds (Å)
CC	1.530
CH	1.090

Table 4
The equilibrium angles in angular bond interaction.

Central atom	Angles (θ)
C-C-C	109.471
C-C-H	109.471
H-C-H	109.471

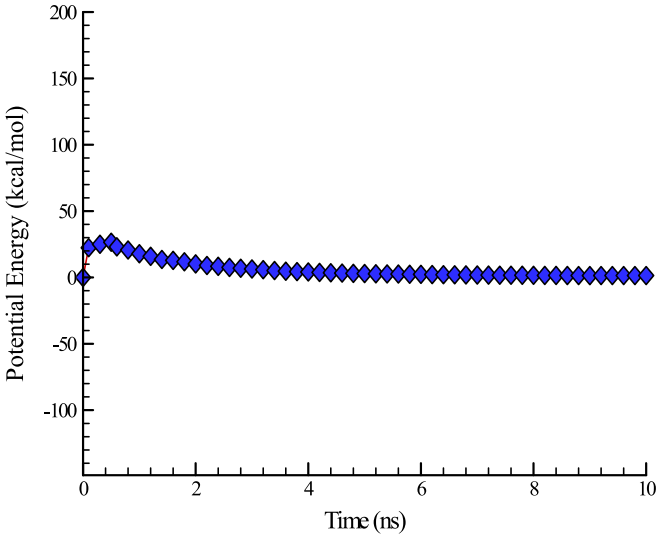

Fig. 2. Variation of potential Energy during 10 ns simulation.

4. Results and discussion

In this section, the effect of the number of rotating ribs on the atomic structure and thermophysical properties of PCM containing 7% Cu nanoparticles was investigated. Fig. 4 illustrates the variation in D as a function of rib number. Quantitatively, increasing the number of rotating ribs from 1 to 4 led to a slight decrease in the maximum D from 0.0856 to 0.0850 atoms/Å^3. This reduction can be attributed to rib-induced perturbations in atomic motion, which enhance V fluctuations and increase intermolecular separation within the confined nanochannel. As the number of ribs increases, more frequent disturbances in atomic trajectories disrupted local packing arrangements, leading to the formation of transient low-D regions. These effects arose from increased atomic mobility and kinetic energy, which promoted spatial redistribution of particles and slightly expanded the effective occupied volume. In addition, the enhanced atomic mobility contributed to a more uniform spatial distribution of nanoparticles within the PCM matrix.

Fig. 5 presents the variation in the maximum V of PCM–Cu nanoparticles as a function of the number of rotating ribs. The results indicate that increasing the rib number from 1 to 4 increased particle V from 0.00481 to 0.00511 Å/fs. This increase was attributed to rib-induced perturbations in atomic motion, which enhanced V fluctuations and momentum exchange within the confined nanochannel. As the number of ribs increased, disturbances in atomic trajectories became more frequent, leading to greater redistribution of kinetic energy among particles. These perturbations disrupted the local atomic equilibrium arrangement and promoted increased atomic mobility within the system. In addition, the interactions between fluid atoms and rotating rib surfaces contributed to localized momentum transfer, further accelerating particle dynamics. Consequently, the increased atomic mobility

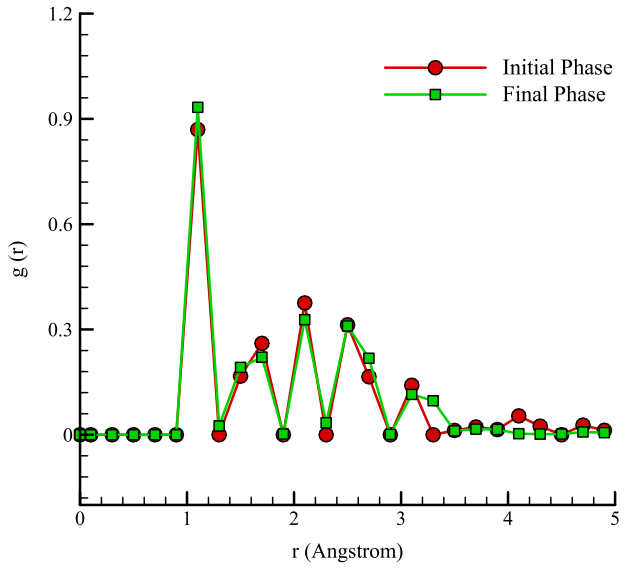

a)

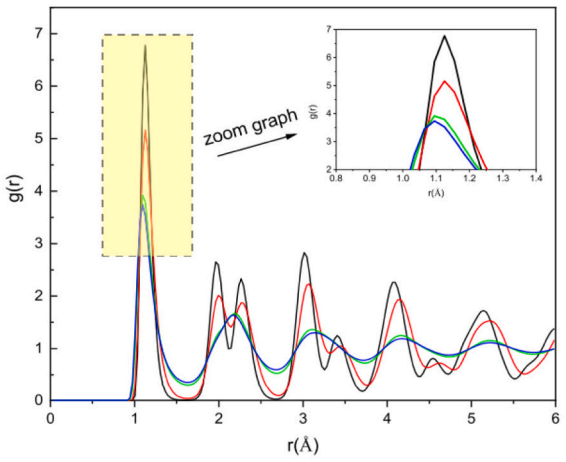

b)

Fig. 3. RDF of paraffin structure at (a) initial and final phases in this study, and (b) comparison with the referenced study [37].

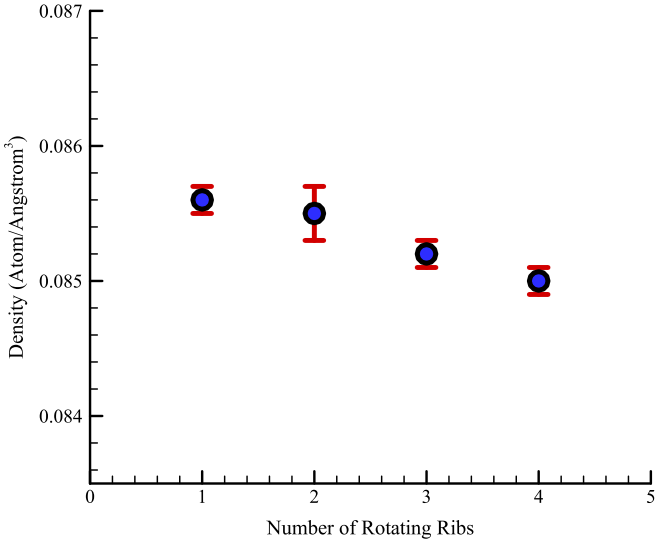

Fig. 4. D variation with rib numbers in the sample.

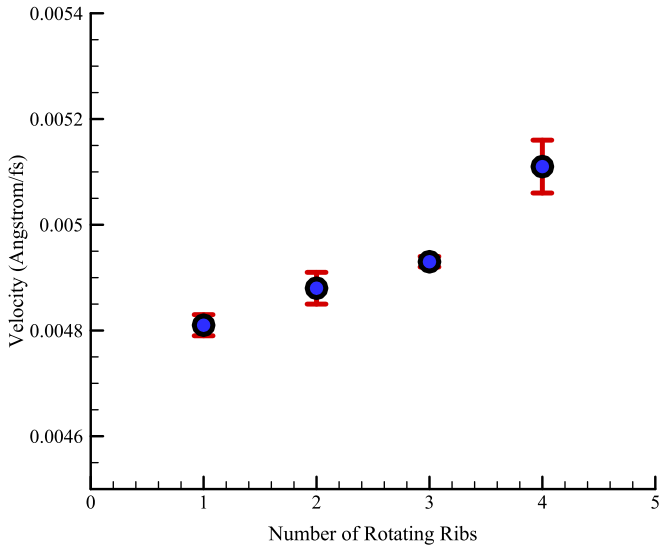

Fig. 5. V variation with rib numbers in the sample.

enhanced energy transfer efficiency at the nanoscale, contributing to the observed improvement in thermal transport properties.

Fig. 6 presents the variation in the maximum T of PCM–Cu nanoparticles as a function of the number of rotating ribs. The results show that increasing the number of ribs from 1 to 4 led to an increase in maximum T from 762 K to 780 K. This T rise was attributed to rib-induced perturbations in atomic motion, which enhanced V fluctuations and increased kinetic energy within the confined system. As the number of ribs increased, more frequent disturbances in atomic trajectories promoted intensified intermolecular interactions and momentum exchange, leading to more efficient conversion of externally applied mechanical work into internal energy. In addition, interactions between fluid atoms and rotating rib surfaces contribute to localized energy accumulation, resulting in the formation of transient high-T regions. These effects reflected enhanced energy redistribution at the atomic scale, governed by confinement and interfacial interactions rather than continuum-scale transport mechanisms. The maximum values of simulated parameters of the simulated structure according to the number of rotating ribs are given in Table 5.

In the present MD simulations, the HF and TC were computed using the Green-Kubo method, a statistical mechanics-based equilibrium

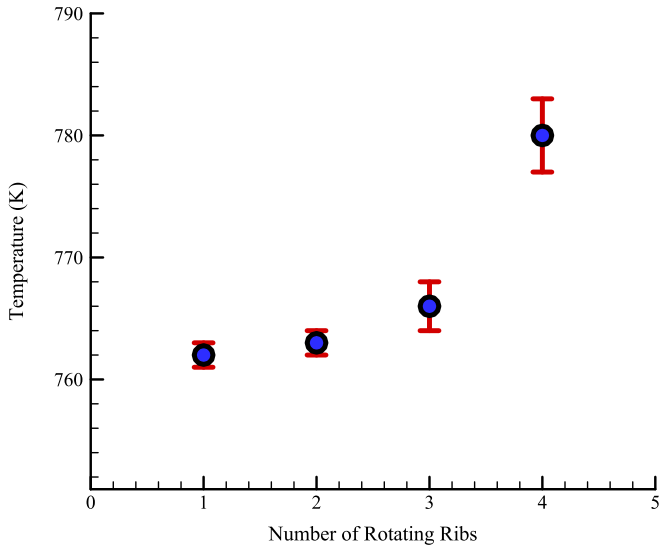

Fig. 6. T variation with rib numbers in the sample.

Table 5
The maximum of simulated parameters of the simulated structure versus the number of rotating ribs.

The number of rotating Ribs	Maximum T (K)	Maximum V (Å/fs)	Maximum D (atom/Å^3)
1	762 ± 1	0.00481 ± 0.00002	0.0856 ± 0.0001
2	763 ± 1	0.00488 ± 0.00003	0.0855 ± 0.0002
3	766 ± 2	0.00493 ± 0.00001	0.0852 ± 0.0001
4	780 ± 3	0.00511 ± 0.00005	0.0850 ± 0.0001

approach. This method calculated TC from the time integral of the HF autocorrelation function at equilibrium, without imposing an external T gradient. HF itself was computed in LAMMPS using the compute heat/flux command, which provided the instantaneous microscopic HF vector derived from atomic energies and atomic-level virial stresses. This function is represented as follows [41]:

$$k = \frac{V}{k_B T^2} \int_0^\infty \langle J_x(0) J_x(t) \rangle dt = \frac{V}{3k_B T^2} \int_0^\infty \langle J(0) . J(t) \rangle dt \quad (6)$$

In the x-direction, $J_x(0)$ and $J_x(t)$ display the heat HF currents at every time and the simulation's initial moment. On the other hand, the sentence inside the integral referred to the average HF function. HF

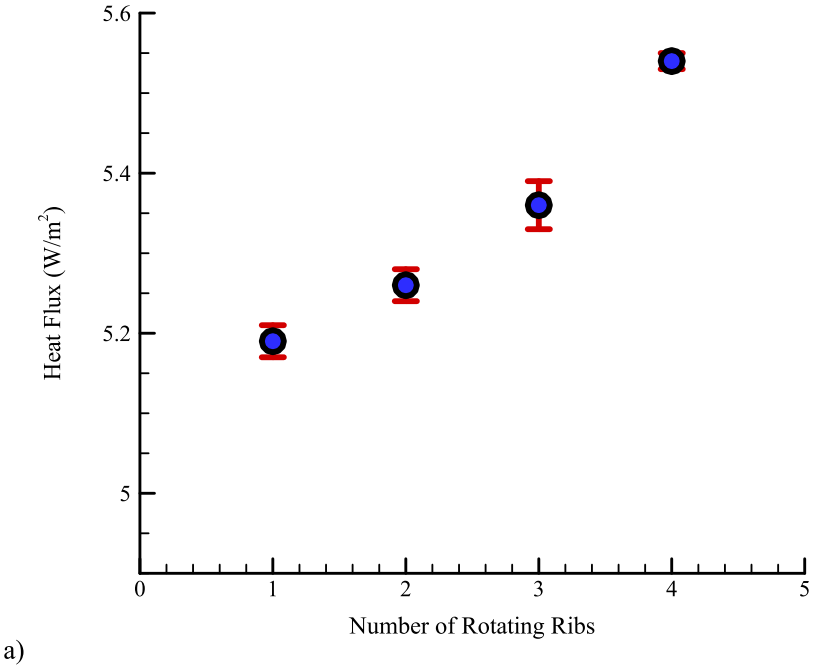

a)

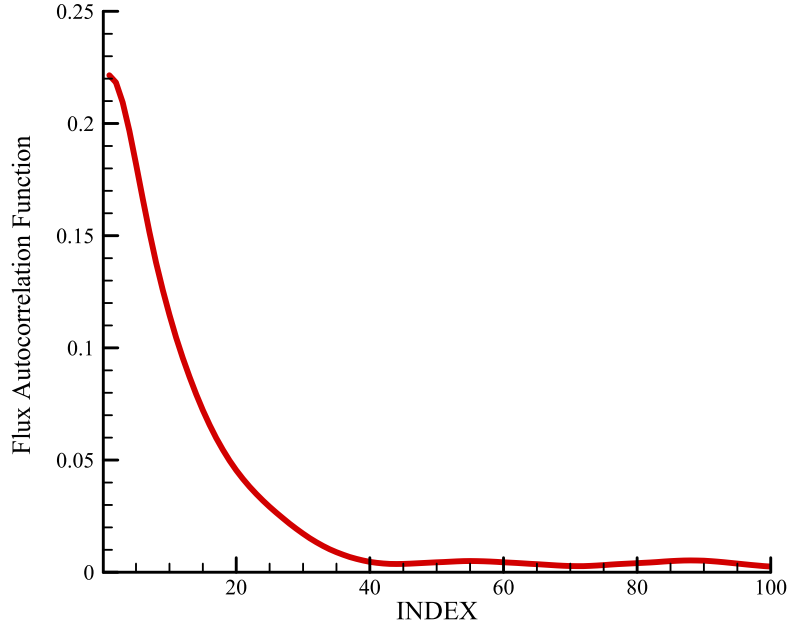

b)

Fig. 7. a) HF variation with the number of ribs in the sample. b) The heat flux autocorrelation function output of the Green-Kubo calculation for the pristine system (modeled sample with one rotating rib). (For interpretation of the references to colour in this figure legend, the reader is referred to the web version of this article.)

vector is obtained from the following equation:

$$J = \frac{1}{V}\left[\sum_i e_i v_i - \sum_i S_i v_i\right]$$

$$= \frac{1}{V}\left[\sum_i e_i v_i - \sum_{i<j}\left(f_{ij} v_j\right) x_{ij}\right] \quad (7)$$

$$= \frac{1}{V}\left[\sum_i e_i v_i - \frac{1}{2}\sum_{i<j}\left(f_{ij}.(v_i + v_j) x_{ij}\right]\right.$$

This method was previously used in research with satisfactory performance [42–44]. Regarding the potential forms, HF in LAMMPS combined the contributions from LJ and Coulombic potentials within a single expression. Hence, the calculated HF accounted for both van der Waals and electrostatic interactions concurrently. The Green-Kubo approach estimates transport properties from equilibrium fluctuations, without applying an external T gradient or an imposed HF (as in NEMD methods).

Fig. 7a presents the variation in HF with increasing number of rotating ribs. The results show that as the number of ribs increased from 1 to 4, the HF rose from 5.19 to 5.54 W/m^2. To ensure the convergence of our thermal calculations using the Green-Kubo method, the heat-flux autocorrelation function was analyzed. The output and convergence of them for the pristine system (modeled system with one rotating rib) are depicted in Fig. 7b. As shown in this figure, the heat flux autocorrelation function convergence is detected in the current thermal calculation. The enhancement of HF output was attributed to rib-induced perturbations in atomic motion, which increased V fluctuations and promoted more frequent intermolecular interactions within the confined nanochannel. The higher rib D led to stronger interactions between fluid atoms and rib surfaces, resulting in greater momentum exchange and more effective energy redistribution at the atomic scale. These effects facilitated more efficient energy transfer across the system and contributed to the observed increase in HF. The results indicate that internal geometric features can significantly influence thermal transport behavior under nanoscale confinement. Similar trends were reported in previous studies, where structured geometries were shown to enhance thermal transport in phase change systems [45]. For instance, Yang et al. [46] demonstrated that the incorporation of rib-like structures can improve the thermophysical performance of composite PCMs by enhancing interfacial interactions. Thermal quantities according to the number of rotating ribs are given in Table 6.

Fig. 8a presents the variation in TC with increasing number of rotating ribs. The results show that as the number of ribs increased from 1 to 4, TC rose from 0.65 to 0.72 W/m·K. This enhancement was attributed to rib-induced perturbations in atomic motion, which increased V fluctuations and promoted more frequent intermolecular interactions within the confined nanochannel. The higher rib D intensified interactions among fluid atoms, nanoparticles, and rib surfaces, thereby enhancing momentum exchange and more efficiently enabling energy transfer pathways. In nanoparticle-enhanced PCMs, TC was strongly influenced by nanoparticle dispersion and interfacial interactions. The presence of rotating ribs increased atomic mobility and improved the spatial distribution of nanoparticles, thereby creating a more effective network for energy transport. To better analyze the physical analysis of the heat transfer process inside the modeled system, the interaction energy between the pristine paraffin sample and NPs was calculated and depicted in Fig. 8 b. As shown in this figure, the magnitude of the mean interaction energy between the paraffin sample and NPs increased to −3.22 kcal/mol by increasing the number of ribs to 4. This energy evolution indicated that the energy exchange between the pristine heat transfer system and NPs was more intense in the presence of a higher number of ribs. So, the heat transfer process occurred more efficiently by adding rotating ribs inside the designed atomic sample, which arises from better interaction in the paraffin-NPs system. At the atomic scale, thermal conduction occurs through energy transfer via molecular interactions in fluids and via vibrational energy exchange (phonon-like mechanisms) in solids. The rotating ribs modified local

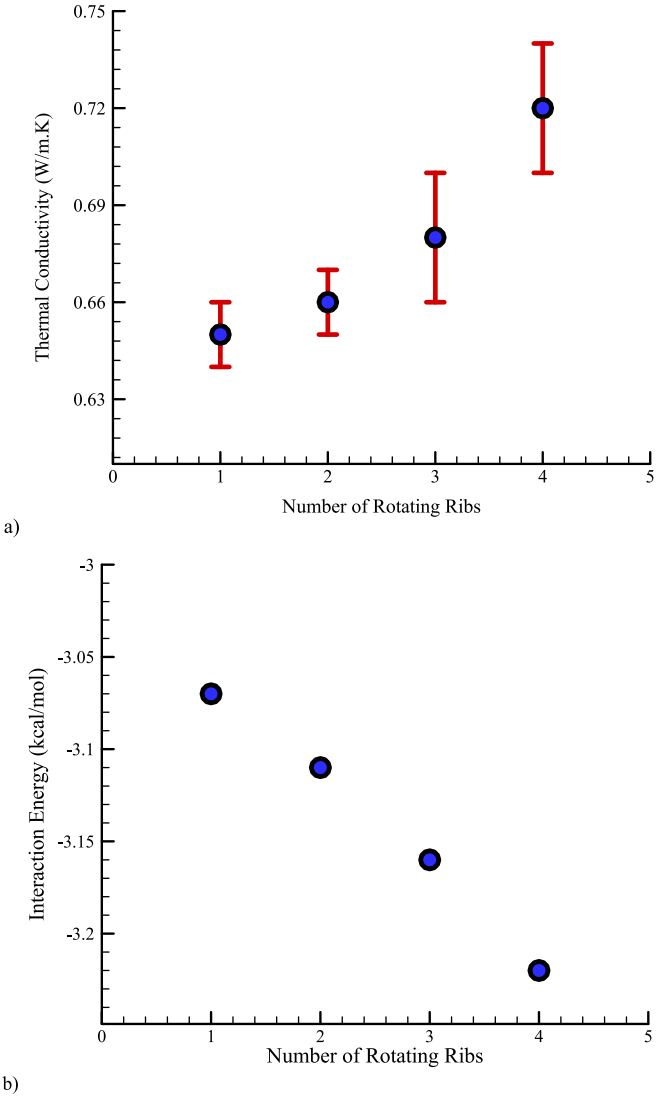

Fig. 8. a) TC variation with rib numbers in the sample. b) Interaction energy between paraffin and NPs variation with rib numbers in the sample.

Table 6
Thermal quantities according to the number of rotating ribs.

The number of rotating Ribs	HF (W/m^2)	TC (W/m.K)	Interaction Energy (kcal/mol)	CT (ns)	DT (ns)
1	5.19 ± 0.02	0.65 ± 0.01	−3.07	6.28 ± 0.01	7.15 ± 0.02
2	5.26 ± 0.02	0.66 ± 0.01	−3.11	6.25 ± 0.02	7.10 ± 0.01
3	5.36 ± 0.03	0.68 ± 0.02	−3.16	6.24 ± 0.01	7.11 ± 0.02
4	5.54 ± 0.01	0.72 ± 0.02	−3.22	6.09 ± 0.04	7.08 ± 0.01

atomic configurations and packing arrangements, increasing the frequency and effectiveness of these interactions. As a result, energy transfer between nanoparticles and surrounding atoms became more efficient, contributing to the observed increase in TC.

The obtained TC range (0.65–0.72 W/m·K) was consistent with previously reported values for nanoparticle-enhanced paraffin systems. For example, Gogoi et al. [47] reported a TC of approximately 0.6 W/m·K for paraffin composites containing carbon nanoparticles, while other studies reported values near 0.7 W/m·K for nanoparticle-reinforced paraffin [48]. Also, the nanoscale reports presented similar TC outputs for thermally improved paraffin nanosystems. Bora et al. [49] reported 0.71 W/m.K for TC of the nanoparticle-enhanced paraffin system. The nanoscale interfacial effects were characterized in their research. Minor differences can be attributed to variations in nanoparticle type, concentration, dispersion state, and methodological approaches. These comparisons supported the reliability of the present results and confirmed the roles of nanoparticle additives and internal structural features in enhancing thermal transport at the nanoscale. Furthermore, consistency between current computational outputs for thermal constants and previous reports validated our simulation settings, such as the used force field and atomic modeling process, under defined conditions.

Fig. 9 illustrates the variation in phase CT with increasing number of rotating ribs. The results show that as the rib number increased from 1 to 4, CT decreased from 6.28 to 6.09 ns. This reduction was attributed to rib-induced perturbations in atomic motion, which enhanced V fluctuations and increased intermolecular interactions within the confined nanochannel. As a result, energy redistribution within the system became more efficient, facilitating faster molecular rearrangements during the phase transition. In addition, the increased number of ribs promoted a more uniform spatial distribution of nanoparticles and strengthened momentum exchange between particles, thereby accelerating structural evolution at the atomic scale. It should be noted that the absolute timescale reported here was specific to the nanoscale simulation domain and captured atomistic transition dynamics rather than macroscopic phase-change durations. The observed reduction in CT therefore, represented a relative acceleration of phase transition kinetics at the atomic level, providing insight into how internal geometric features influenced energy transfer and structural evolution under confined conditions.

Fig. 10 presents the variation in DT with increasing number of rotating ribs. The results show that as the number of ribs increased from 1 to 4, DT decreased from 7.15 to 7.08 ns. This reduction was attributed

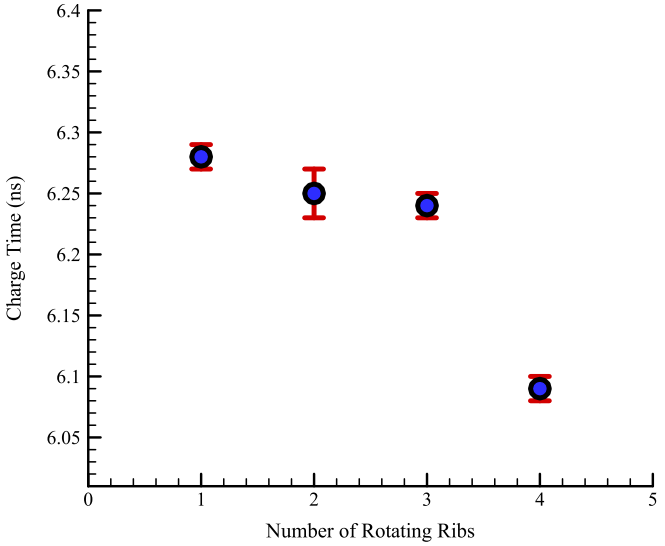

Fig. 9. CT variation with rib numbers in the sample.

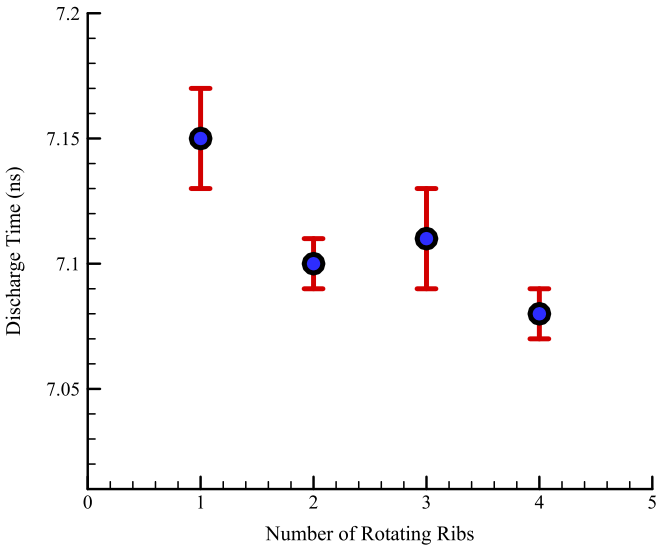

Fig. 10. DT variation with rib numbers in the sample.

to rib-induced perturbations in atomic motion, which enhanced V fluctuations and increased intermolecular interactions within the confined nanochannel. As a result, energy redistribution became more efficient, facilitating faster structural reorganization during solidification. In addition, the increased rib number promoted a more uniform spatial distribution of nanoparticles and strengthened momentum exchange among particles, further contributing to accelerated phase transition kinetics. It should be noted that the absolute timescale reported here was characteristic of atomistic simulations and showed nanoscale transition dynamics rather than macroscopic cooling durations. The observed decrease in DT therefore showed a relative enhancement in phase transition kinetics (~1%), providing insight into how internal geometric features influenced energy transfer and structural evolution under confined conditions.

5. Conclusion

This study examined the effect of unconnected rotating ribs on the thermophysical behavior of nanoparticle-enhanced phase change materials (NePCMs) confined within nanochannels using MD simulations. The results show that increasing the number of ribs altered the local atomic environment and strengthened fluid–solid interactions, leading to increased atomic mobility, improved nanoparticle dispersion, and more frequent intermolecular interactions within the confined domain. Consequently, enhanced HT behavior and a slight reduction in phase transition time were observed. At the atomic scale, these enhancements originated from rib-induced perturbations in particle motion, which increased V fluctuations and momentum exchange, thereby promoting more effective energy redistribution and facilitating molecular rearrangements during the phase transition process. These effects were governed by confinement and interfacial interactions rather than continuum-scale transport mechanisms. A consistent enhancement trend was observed, corresponding to a relative increase of approximately 6–11% in thermal transport properties with increasing rib number, confirming the systematic influence of internal geometric features at the nanoscale. Periodic boundary conditions were employed to minimize finite-size effects and represent an effectively extended system; however, the simulations remained inherently atomistic. Therefore, the reported thermophysical values were not directly transferable to macroscopic systems. Instead, the findings provide fundamental insight into the role of nanoscale geometry and confinement in governing HT and phase transition behavior.

5.1. Future suggestion

Future work should focus on extending these atomic-scale insights to larger-scale and more complex geometries, exploring different nanoparticle materials and concentrations, and investigating dynamic operating conditions to fully realize the potential of ribbed nanochannel configurations in practical applications.

CRediT authorship contribution statement

Jialing Li: Investigation, Funding acquisition, Writing – original draft, Writing – review & editing, Conceptualization. **Xiaogui Gou:** Writing – original draft, Software, Validation. **Mahmut Taner:** Investigation, Funding acquisition. **Soheil Salahshour:** Investigation, Funding acquisition, Writing – review & editing, Conceptualization. **N. Emami:** Investigation, Funding acquisition, Writing – original draft, Writing – review & editing, Conceptualization. **Mustafa Bayram:** Software, Validation, Conceptualization.

Consent for publication

N/A

Ethics approval and consent to participate

N/A

Funding declaration

Not Applicable.

Declaration of competing interest

The authors declare that they have no known competing financial interests or personal relationships that could have appeared to influence the work reported in this paper.

Acknowledgments

N/A

Data availability

No data was used for the research described in the article.

References

[1] R. Abaszade, E. Khanmamadova, Fundamentals of thermal management in renewable energy systems, in: Heat Exchanger Technologies for Sustainable Renewable Energy Systems, CRC Press, 2025, pp. 30–51.
[2] V.H.U. Eze, J.S. Tamball, O.F. Uzoma, I. Sarah, O. Robert, W. Okafor, Advancements in energy efficiency technologies for thermal systems: a comprehensive review, INOSR Appl. Sci. 12 (1) (2024) 1–20.
[3] G. Rasool, W. Xinhua, T. Sun, T. Hayat, M. Sheremet, A. Uddin, H. Shahzad, K. Abbas, I. Razzaq, W. Yuexin, Recent advancements in battery thermal management system (BTMS): a review of performance enhancement techniques with an emphasis on nano-enhanced phase change materials, Heliyon 10 (17) (2024).
[4] M. Ohring, L. Kasprzak, Reliability and Failure of Electronic Materials and Devices, Academic Press, 2014.
[5] L. Yang, H. Yan, J.C. Lam, Thermal comfort and building energy consumption implications–a review, Appl. Energy 115 (2014) 164–173.
[6] K. Yuan, J. Shi, W. Aftab, M. Qin, A. Usman, F. Zhou, Y. Lv, S. Gao, R. Zou, Engineering the thermal conductivity of functional phase-change materials for heat energy conversion, storage, and utilization, Adv. Funct. Mater. 30 (8) (2020) 1904228.
[7] S.R. Chalivendula, H. Tarigonda, Recent advances in organic phase change materials for thermal energy storage: a review on sustainable development applications, Int. J. Thermophys. 46 (6) (2025) 1–56.
[8] Y. Li, Z. Fu, M. Xue, Z. Shao, Y. Li, Q. Zhu, Experimental study on preparation and thermal storage properties of expanded graphite/paraffin wax as a shape-stabilized phase change material, Energy Rep. 8 (2022) 324–331.
[9] J. Li, S. Mo, Z. Zhou, Y. Du, L. Jia, Y. Chen, Nanoparticle-enhanced phase change materials for thermal energy storage: a critical review, Renew. Sustain. Energy Rev. 223 (2025) 116040.
[10] A. Agarwal, M.K.W. Kalenga, M. Ilunga, Thermal characterization of structured porous materials and phase change composites for heat sink applications, Processes 13 (5) (2025) 1606.
[11] Y. Ru, A.B. Ali, K.H. Qader, R.A. Hussein, R. Jhala, M. Soliyeva, S. Salahshour, M. Hekmatifar, Effect of nanoparticle size on the thermal performance of paraffin-O2 hybrid heat sink using molecular dynamics approach, Int. Commun. Heat Mass Transfer 163 (2025) 108713.
[12] Q. An, M. Bagheritabar, A. Basem, A.A. Ghabra, Y. Li, M. Tang, L.S. Sabri, R. Sabetvand, The effect of size of copper oxide nanoparticles on the atomic and thermal behavior of silica aerogel/paraffin nanostructure in a cylindrical duct using molecular dynamics simulation, Case Stud. Therm. Eng. (2024) 104666.
[13] C. Zhao, C. Yang, Y. Tao, Y. He, Interfacial nanolayer effect on thermophysical properties of silica-paraffin phase change material-a molecular dynamics simulation, Int. J. Heat Mass Transf. 220 (2024) 125007.
[14] C. Wu, Q. Wang, X. Wang, S. Sun, J. Bai, D. Cui, S. Pan, H. Sheng, Effect of Al2O3 nanoparticle dispersion on the thermal properties of a eutectic salt for solar power applications: experimental and molecular simulation studies, Energy 288 (2024) 129785.
[15] M.D. Hanwell, D.E. Curtis, D.C. Lonie, T. Vandermeersch, E. Zurek, G.R. Hutchison, Avogadro: an advanced semantic chemical editor, visualization, and analysis platform, J. Chem. 4 (2012) 1–17.
[16] L. Martínez, R. Andrade, E.G. Birgin, J.M. Martínez, PACKMOL: a package for building initial configurations for molecular dynamics simulations, J. Comput. Chem. 30 (13) (2009) 2157–2164.
[17] A.P. Thompson, H.M. Aktulga, R. Berger, D.S. Bolintineanu, W.M. Brown, P. S. Crozier, P.J. In't Veld, A. Kohlmeyer, S.G. Moore, T.D. Nguyen, LAMMPS-a flexible simulation tool for particle-based materials modeling at the atomic, meso, and continuum scales, Comput. Phys. Commun. 271 (2022) 108171.
[18] P.L. Barclay, D.Z. Zhang, Periodic boundary conditions for arbitrary deformations in molecular dynamics simulations, J. Comput. Phys. 435 (2021) 110238.
[19] S. Gravelle, J.R. Gissinger, A. Kohlmeyer, A Set of Tutorials for the LAMMPS Simulation Package, arXiv preprint arXiv:2503.14020, 2025.
[20] Y. Zou, J. Cai, X. Huai, F. Xin, Z. Guo, Molecular dynamics simulation of heat conduction in Si nano-films induced by ultrafast laser heating, Thin Solid Films 558 (2014) 455–461.
[21] X. Wang, X. Xu, Molecular dynamics simulation of thermal and thermomechanical phenomena in picosecond laser material interaction, Int. J. Heat Mass Transfer 46 (1) (2003) 45–53.
[22] X.-B. Mi, A.T. Chwang, Molecular dynamics simulations of nanochannel flows at low Reynolds numbers, Molecules 8 (1) (2003) 193–206.
[23] C. Soong, T. Yen, P. Tzeng, Molecular dynamics simulation of nanochannel flows with effects of wall lattice-fluid interactions, Phys. Rev. E—Stat. Nonlinear Soft Matter Phys. 76 (3) (2007) 0363, 03.
[24] V. Bitrián, J. Principe, Driving mechanisms and streamwise homogeneity in molecular dynamics simulations of nanochannel flows, Phys. Rev. Fluids 3 (1) (2018) 014202.
[25] M. Ishida, T. Ohba, Hybrid reverse molecular dynamics simulation as new approach to determination of carbon nanostructure of carbon blacks, Sci. Rep. 10 (1) (2020) 3622.
[26] S.L. Mayo, B.D. Olafson, W.A. Goddard, DREIDING: a generic force field for molecular simulations, J. Phys. Chem. 94 (26) (1990) 8897–8909.
[27] A.K. Rappé, C.J. Casewit, K. Colwell, W.A. Goddard III, W.M. Skiff, UFF, a full periodic table force field for molecular mechanics and molecular dynamics simulations, J. Am. Chem. Soc. 114 (25) (1992) 10024–10035.
[28] S. Solhjoo, A.I. Vakis, Definition and detection of contact in atomistic simulations, Comput. Mater. Sci. 109 (2015) 172–182.
[29] J.E. Lennard-Jones, Cohesion, Proc. Phys. Soc. 43 (5) (1931) 461.
[30] P.G. Huray, Maxwell's Equations, John Wiley & Sons, 2009.
[31] D.C. Rapaport, The Art of Molecular Dynamics Simulation, Cambridge university press, 2004.
[32] Y. Li, X. Jin, E. Moubarak, B. Smit, A refined set of universal force field parameters for some metal nodes in metal–organic frameworks, J. Chem. Theory Comput. 20 (23) (2024) 10540–10552.
[33] P.G. Boyd, S.M. Moosavi, M. Witman, B. Smit, Force-field prediction of materials properties in metal-organic frameworks, J. Phys. Chem. Lett. 8 (2) (2017) 357–363.
[34] Copyright 2003-2026 Sandia Corporation, https://docs.lammps.org/bond_harmonic.html.
[35] Copyright 2003-2026 Sandia Corporation, https://docs.lammps.org/angle_harmonic.html.
[36] T. Raček, O. Schindler, D. Toušek, V. Horský, K. Berka, J. Koča, R. Svobodová, Atomic charge calculator II: web-based tool for the calculation of partial atomic charges, Nucleic Acids Res. 48 (W1) (2020) W591–W596.
[37] J. Cao, L. Liu, C. Liu, C. He, Phase transition mechanisms of paraffin in waxy crude oil in the absence and presence of pour point depressant, J. Mol. Liq. 345 (2022) 116989.
[38] A.S. Gangan, E.D. Cubuk, S.S. Schoenholz, M. Bauchy, N.A. Krishnan, Force-field optimization by end-to-end differentiable atomistic simulation, J. Chem. Theory Comput. 21 (12) (2025) 5867–5879.
[39] S. Chiba, Y. Okuno, T. Honma, M. Ikeguchi, Force-field parametrization based on radial and energy distribution functions, J. Comput. Chem. 40 (29) (2019) 2577–2585.

[40] A.D. Wade, L.-P. Wang, D.J. Huggins, Assimilating radial distribution functions to build water models with improved structural properties, J. Chem. Inf. Model. 58 (9) (2018) 1766–1778.
[41] D. Frankel, B. Smit, Molecular Simulation: From Algorithm to Applications, Second edition, Academic Press, 2002.
[42] V.M. Nazarychev, A.D. Glova, I.V. Volgin, S.V. Larin, A.V. Lyulin, S.V. Lyulin, A. A. Gurtovenko, Evaluation of thermal conductivity of organic phase-change materials from equilibrium and non-equilibrium computer simulations: paraffin as a test case, Int. J. Heat Mass Transfer 165 (2021) 120639.
[43] A. Jain, S. McGinty, G. Pontrelli, L. Zhou, Theoretical modeling of endovascular drug delivery into a multilayer arterial wall from a drug-coated balloon, Int. J. Heat Mass Transfer 187 (2022) 122572.
[44] T.A. Tabish, R.J. Narayan, M. Edirisinghe, Rapid and label-free detection of COVID-19 using coherent anti-Stokes Raman scattering microscopy, MRS Commun. 10 (4) (2020) 566–572.
[45] Z. Yao, C. Yang, B. Chen, G. Dai, Y. Chen, Computational fluid dynamics analysis of PCM-based ocean thermal engine with external rib turbulators, Appl. Therm. Eng. 238 (2024) 122054.
[46] X. Yang, X. Zheng, Z. Yang, Y. Bai, H. Chen, Effects of morphology and internal voids of copper ribs on heat transfer performance in copper foam/paraffin composite phase change materials, Int. J. Heat Mass Transf. 152 (2020) 119526.
[47] M. Gogoi, B. Das, P.K. Patowari, Thermal Conductivity Enhancement of a Paraffin Wax-Based Composite Phase Change Material for Energy Storage, 2024. Available at SSRN 4753820.
[48] L.-W. Fan, X. Fang, X. Wang, Y. Zeng, Y.-Q. Xiao, Z.-T. Yu, X. Xu, Y.-C. Hu, K.-F. Cen, Effects of various carbon nanofillers on the thermal conductivity and energy storage properties of paraffin-based nanocomposite phase change materials, Appl. Energy 110 (2013) 163–172.
[49] N. Bora, D.P. Joshi, Enhancement in thermal properties of organic phase change material (paraffin) via TiO2 foam doping, Prabha Mater. Sci. Lett. 2 (1) (2023) 1–15.